

# Mapping Residual Stress Distributions at the Micron Scale in Amorphous Materials

BARTLOMIEJ WINIARSKI, RICHARD M. LANGFORD, JIAWAN TIAN, YOSHIHIKO YOKOYAMA, PETER K. LIAW, and PHILIP J. WITHERS

Residual stresses in crystalline or glassy materials often play a key role in the performance of advanced devices and components. However, stresses in amorphous materials cannot easily be determined at the micron scale by diffraction, or by other conventional laboratory methods. In this article, a technique for mapping residual stress profiles in amorphous materials with high spatial definition is presented. By applying a focused ion beam (FIB)-based semidestructive mechanical relaxation method, the stresses are mapped in a peened and fatigued bulk metallic glass (BMG) ( $Zr_{50}Cu_{40}Al_{10}$  at. pct). The residual stresses are inferred using finite element analysis (FEA) of the surface relaxations, as measured by digital image correlation (DIC), that occur when a microslot is micromachined by FIB. Further, we have shown that acceptable accuracy can in most cases be achieved using a simple analytical model of the slot. It was found that the fatigue cycling significantly changes the distribution of compressive residual stresses with depth in the plastically deformed surface layer. Our observations point to the scalability of this method to map residual stresses in volumes as small as  $1 \times 1 \times 0.2 \mu\text{m}^3$  or less.

DOI: 10.1007/s11661-009-0127-4

© The Minerals, Metals & Materials Society and ASM International 2009

## I. INTRODUCTION

**BULK** metallic glasses (BMGs)<sup>[1,2]</sup> are attractive materials for high-performance applications in a wide variety of fields.<sup>[3,4]</sup> This is because their microstructures give rise to, among other things, strengths approaching theoretical limits, high hardness,<sup>[5]</sup> good fatigue strengths,<sup>[6]</sup> a uniquely high capacity for elastic energy storage per unit volume, low damping, and remarkable fracture toughness, which distinguish them from other engineering materials.<sup>[7]</sup> However, thermal residual stresses are an unavoidable issue<sup>[8]</sup> due to the fast cooling rates needed to retain a glassy structure on cooling. Furthermore, these residual stresses have been shown to have significant effects on their mechanical behavior.<sup>[9–11]</sup> Consequently, an accurate means of assessing residual

stresses is essential not only for understanding how they affect the mechanical behavior of BMGs, but also to guide the tailoring of residual stress levels through subsequent processing treatments such as shot peening.<sup>[9]</sup> Unfortunately, stresses in amorphous materials cannot easily be determined at the micron scale by conventional laboratory methods, either by destructive methods (too coarse), or conventional X-ray diffraction analyses (amorphous). As a result, stress measurements in metallic glasses in general and those relating to peening, in particular, are sparse.<sup>[12]</sup>

Residual stresses are those stresses that are retained within a material when no external forces are acting. Depending on their sign, magnitude, spatial distribution, and the scale over which they equilibrate, residual stresses can alter the component performance and promote/inhibit failure processes.<sup>[13]</sup> As stated earlier, quench stresses are an inevitable outcome of metallic glass production, while thermal tempering is regularly used to introduce a beneficial residual stress profile (compressive surface residual stresses balanced by the midplane tension) into silicate glasses<sup>[14]</sup> and BMGs.<sup>[15,16]</sup> Favorable compressive residual stresses can also be generated by introducing surface plastic deformation, for example, by shot peening (bombarding the surface with small “shot”). This surface engineering process can enhance the ductility of BMGs, depending on the load case.<sup>[9]</sup> In tension, the compressive residual stresses inhibit early crack propagation, while in compression, the compressive residual stresses can combine with pre-existing shear bands in the surface layer to facilitate finer and more uniform shear banding. Thus, the premature failure on a few dominant shear bands is suppressed, and homogeneous plastic deformation can be sustained.<sup>[9,17]</sup> While the surface stresses have a major effect on the fatigue

---

BARTLOMIEJ WINIARSKI, Postdoctoral Research Associate, and PHILIP J. WITHERS, Professor, are with the School of Materials, The University of Manchester, Grosvenor St, Manchester, M1 7HS, United Kingdom. Contact e-mail: philip.withers@manchester.ac.uk RICHARD M. LANGFORD, formerly Senior Experimental Officer, with the School of Materials, The University of Manchester, is Facility Manager, Electron Microscopy Suite, The Cavendish Laboratory, University of Cambridge, Cambridge, CB3 0HE, United Kingdom. JIAWAN TIAN, Postdoctoral Scholar, and PETER K. LIAW, Professor and Ivan Racheff Chair of Excellence, are with the Department of Materials Science and Engineering, The University of Tennessee, Knoxville, TN 37996. YOSHIHIKO YOKOYAMA, Associate Professor, is with the Materials Science and Engineering Department, Himeji Institute of Technology, Shosha 2167, Himeji, Japan.

This article is based on a presentation given in the symposium “Bulk Metallic Glasses VI,” which occurred during the TMS Annual Meeting, February 15–19, 2009, in San Francisco, CA, under the auspices of TMS, the TMS Structural Materials Division, TMS/ASM: Mechanical Behavior of Materials Committee.

Article published online December 12, 2009

resistance of metal alloys, BMGs experience only minor enhancements.<sup>[10,18]</sup> To date, our understanding of the influence of residual stresses on the fatigue behavior of BMGs has been held back by a dearth of suitable measurement techniques. The following methods have been applied previously to measure residual stresses in amorphous materials: (1) “hard” X-ray or neutron scattering methods,<sup>[19,20]</sup> (2) the curvature-measurement method,<sup>[9]</sup> and (3) the crack-compliance (incremental slitting) method.<sup>[16]</sup> Although the amorphous X-ray scattering signature is typically broad, Poulsen *et al.*<sup>[19]</sup> used high-energy synchrotron X-ray scattering to measure the strain *via* the radial-distribution function, describing mean atomic separations in an amorphous material with a sensitivity of  $10^{-4}$ . Very recently, the method has been applied to peened layers in BMGs.<sup>[12]</sup> Due to the complexity of the experimental setup and subsequent analysis, the synchrotron diffraction method is far from an everyday laboratory tool and is sensitive to volume changes in the glass, as will be discussed later. Although not as accurate or versatile as crystalline diffraction methods,<sup>[21,22]</sup> curvature measurements<sup>[9]</sup> remain the dominant means of evaluating residual stress in BMGs. When used to determine residual stress variations with depth, such as for shot peening, the thickness of the affected surface layer must be estimated because this method is based upon a thin film model, and the appropriateness of the assumption can have a significant effect on the final results.<sup>[9]</sup> Curvature and crack-compliance methods can be applied with good depth resolution ( $\sim 80$  to  $500 \mu\text{m}$ ) to evaluate the residual stresses averaged over relatively large areas, typically areas having dimensions in millimeters. Using high-resolution wafer curvature techniques, stresses have been inferred at depths of tens of nanometers; however, the residual stresses are averaged across a large area ( $60,000 \times 3000 \mu\text{m}^2$ ).<sup>[23]</sup>

This article describes a new method for mapping the spatial variation in residual stresses with high lateral and depth resolution based on the combined imaging/milling capabilities of a dual-beam focused ion beam (FIB) microscope (FEI DualBeam xT Nova NanoLab 200). This technique is based on the downscaling of the mechanical slotting relaxation method, in which the residual stresses released in the vicinity of a microscale slot are inferred from the local relaxation displacements as measured by digital image correlation (DIC) software. Because of the characteristic milling capabilities of the FIB, a wedge-shaped-slot geometry is obtained. By milling an end trench, we have been able to measure the shape and depth of the slot. We have compared the stresses inferred using an analytical method that treats the slot as an infinitely long and narrow crack<sup>[24]</sup> with that arising from a finite element (FE) model that uses the measured slot geometry. Kang *et al.*<sup>[25]</sup> and Sabaté *et al.*<sup>[26]</sup> have previously used image correlation to measure stresses on the top surface of a coating by relaxation displacement measurements after FIB milling, but our method is the first to provide spatially resolved residual stress data. The method is used to determine the stresses in a surface severely plastically deformed ( $\text{S}^2\text{PD}$ )<sup>[27]</sup>  $\text{Zr}_{50}\text{Cu}_{40}\text{Al}_{10}$  (at. pct) BMG system after failure under four-point-bending fatigue. The

influence of fatigue loading on the spatial resolution of the residual stresses is also studied.

## II. EXPERIMENTAL DESCRIPTION

### A. Material Preparation

The material studied is a Zr-based  $\text{Zr}_{50}\text{Cu}_{40}\text{Al}_{10}$  (at. pct) BMG prepared by arc melting a mixture of pure zirconium, copper, and aluminum melts (purity better than 99.9 pct by weight) in an argon atmosphere. A tilt-casting method was implemented to cast the alloy to its final rod shape of 60 mm and diameter of 8 mm. The rod sample was cut to a rectangular bar  $3 \times 3 \times 25 \text{ mm}^3$  before polishing using 600-grit grinding paper.

### B. $\text{S}^2\text{PD}$ Surface Treatment Process

Prior to fatigue testing, one side of the rod was repeatedly bombarded by 20 WC/Co balls each having a diameter of 1.6 mm using a Spex 8000 miller (SPEX Industries, Inc., Scotch Plains, NJ) in a back-to-force mode at a frequency of 60 Hz in an argon atmosphere. The bombardment process lasted for 180 minutes, pausing every 15 minutes. This  $\text{S}^2\text{PD}$  process has a much higher average impact energy than the conventional shot-peening process, thereby generating a severely deformed near-surface layer in the BMG at room temperature.<sup>[27]</sup>

### C. Fatigue Test

After the  $\text{S}^2\text{PD}$  process, the fatigue behavior of the peened BMG was studied under four-point-bending fatigue (Figure 1(a)). The sample was exposed to a maximum stress of 500 MPa on the top surface with a load ratio (minimum load/maximum load) of 0.1. The sample failed after 52,499 cycles.

### D. Surface Contrast Enhancement for DIC

The reliability of the DIC analysis and the scalability of the FIB-based slitting method strongly depend on the size, distribution, and density of features on the specimen surface.<sup>[28]</sup> This was enhanced by decorating the specimen surface with 20- to 30-nm yttria-stabilized zirconia (YSZ)-equiaxed particles ( $\sim 13$  pct coverage) precipitated from an ethanol suspension (Figure 1(b)). An ultrasonic bath was used to break up large YSZ particle conglomerates in the suspension prior to application.

### E. FIB Slotting Process

The aim was to monitor the distribution of residual stresses along two “lines” (strictly narrow bands, because the slots are slightly displaced laterally from one another) running from the peened (top) surface into the sample, as follows. (1) Line A lies in the region unaffected by the fatigue test; this would be expected to be representative of the as-peened surface. (2) Line B lies

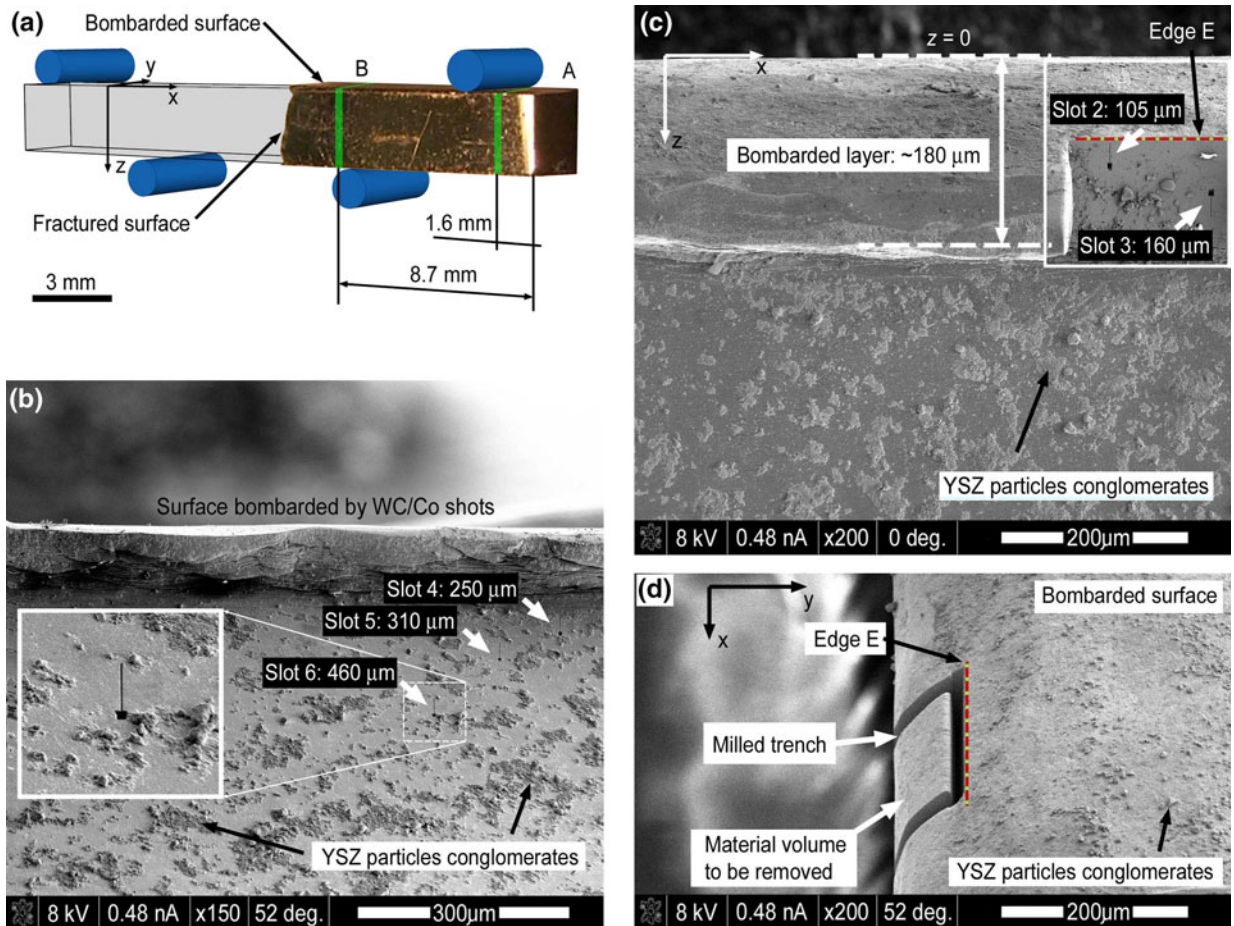


Fig. 1—BMG specimen: (a) general view showing test configuration and location of the regions under investigation; (b) FEGSEM image showing the positions of slots 4 through 6 from the bombarded surface along line B in Fig. 1(a); (c) FEGSEM image showing the corresponding slots 2 and 3 from the peened surface (inset); edge E corresponds to the edge in Fig. 1(d); and (d) FEGSEM image showing the protruding microstructurally affected layer into which a  $(200 \times 100 \times 80\text{-}\mu\text{m}^3)$  trench was excavated to enable milling of slots 2 and 3, region B. Close-ups of slot 1 can be found in Figs. 2 and 3(a).

**Table I. Slot Depths,  $z$  ( $\mu\text{m}$ ), for Lines Marked in Figure 1(a)**

Slot	1	2	3	4	5	6	7
Line A	0	165	240	290	375	680	930
Line B	0	105	160	250	310	460	870

between the fractured surface and an inner roller (Figure 1(a)); this region has been exposed to the full fatigue amplitude.

In order to map the stress distribution along each line, a series of  $(40 \times 4 \times 0.8\text{-}\mu\text{m}^3)$  microslits was progressively milled using a voltage of 30 kV and a current of 280 nA: for each line, one slot was milled on the peened surface itself and a number of others were milled down the side of the specimen at set depths below the deformed surface (Figures 1(b) and (c)). In this manner, the residual stress in the  $x$  direction could be analyzed as a function of depth ( $z$ ) (Figure 1(a)). The slot locations are summarized in Table I. The experimental and analysis procedures for slot 1 on line A are shown in Figures 2 and 3(a), by way of example.

Our FIB slitting method builds on the approach of Kang *et al.*,<sup>[25]</sup> but after slotting, we milled an end trench in order to monitor the depth and shape of each FIB-processed slot (Figure 2). This modification is important because it is not possible to excavate deep microslots having perfectly rectangular walls, and the predefined slot depth may vary substantially from the intended depth. In this way, we were able to assess whether an accurate model of the slot geometry is necessary (Section H). A microstructurally evident (affected) layer arising from the peening process is clearly visible in Figures 1(b) and (c) and extends to a depth of approximately  $180 \mu\text{m}$ . As is evident, this layer protruded from the side of the bar and was not suitable for slotting. Instead, a material volume of approximately  $200 \times 100 \times 80 \mu\text{m}^3$  was excavated by FIB milling in order to present a suitable surface over this region (Figure 1(d)).

#### F. Displacement Mapping by DIC

Surface displacements due to the stress relaxation were measured for each microslot by DIC analysis. The



displacement accuracy depends on the surface contrast as well as the vector calculation parameters (VCPs) used during the cross-correlation analysis, in this case obtained using LaVision DaVis 7.2 software\*. During

\*LaVision DaVis is a trademark of LaVision GmbH, Goettingen, Germany.

the analysis, images are divided into smaller subregions (patches), which are individually correlated.<sup>[28]</sup>

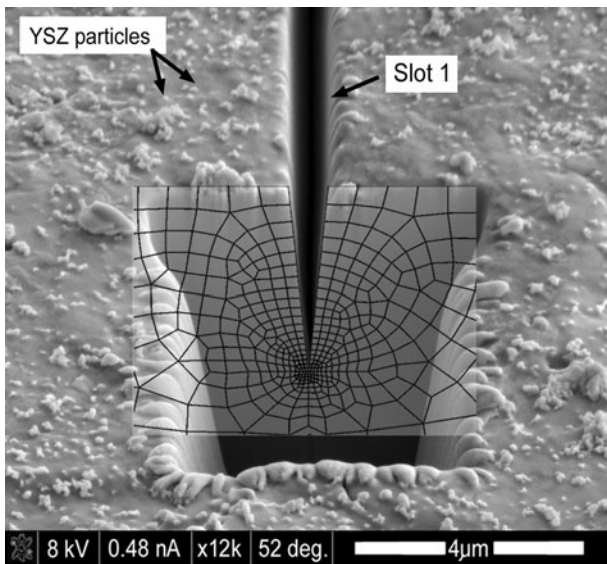


Fig. 2—FEGSEM image showing the slot cross section (slot 1, region A) as revealed by a subsequent observational trench excavated at one end of the slot (depth  $a = 4.1 \pm 0.09 \mu\text{m}$ , width  $w = 0.8 \pm 0.06 \mu\text{m}$ , and length  $l = 40 \pm 0.06 \mu\text{m}$ ). The FEA model of the slot is superimposed.

Before analyzing all the slotting experiments, the best VCPs were determined from two field emission gun scanning electron microscope (FEGSEM) images captured before the slotting by quantifying the accuracy of the displacement field measurement  $\delta u_x$  in the green box region shown in Figure 3(a). The accuracy of the displacement field measurement is defined as

$$\delta u_x = (L_x/M_x)k \quad [1]$$

where  $L_x$  is the micrograph size in micrometers in the horizontal ( $x$ ) direction,  $M_x$  is the corresponding number of pixels in the  $x$  direction, and  $k$  is the subpixel resolution, calculated as the standard deviation of the displacement field over the mapped green box region. The subpixel resolution is a major benchmark for the precision of the displacement measurements.

The FEGSEM imaging conditions are summarized in Table II. The image correlation parameters (VCPs) were varied to optimize spatial and displacement resolution. The results of the accuracy analysis of the displacement measurement for the selected VCPs for slot 1 (line A) are summarized in Table III. While the VCPs corresponding to set C appear to have slightly better accuracy than for set D, set D gives more vectors and is, statistically speaking, likely to be more reliable. Thus, set D represents a good compromise between the spatial resolution and the strain resolution ( $64 \times 64$  pixels and 75 pct patch overlap). In order to measure the relaxation displacements associated with the FIB milling

Table II. FEGSEM Imaging Conditions

Voltage (kV)	Current (nA)	Magnification	Detector	Image Size (Pixels)
8	0.48	3500	ETD (SE)*	1024 × 884

\*Everhart Thornley (FEI DualBeam xT Nova NanoLab 600, FEI Company, Hillsboro, OR) secondary electron detector.

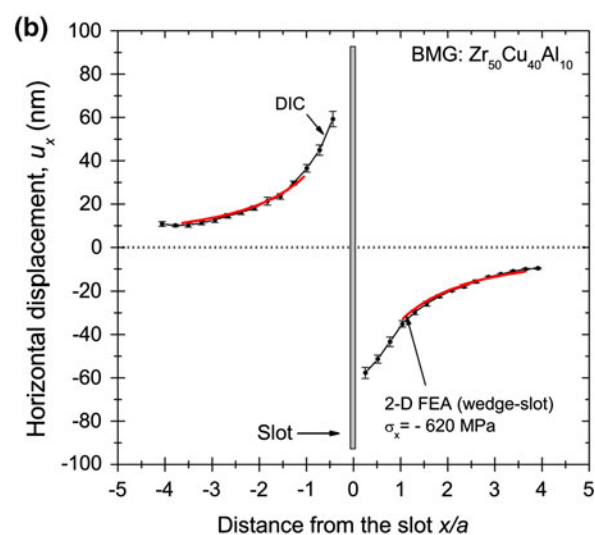
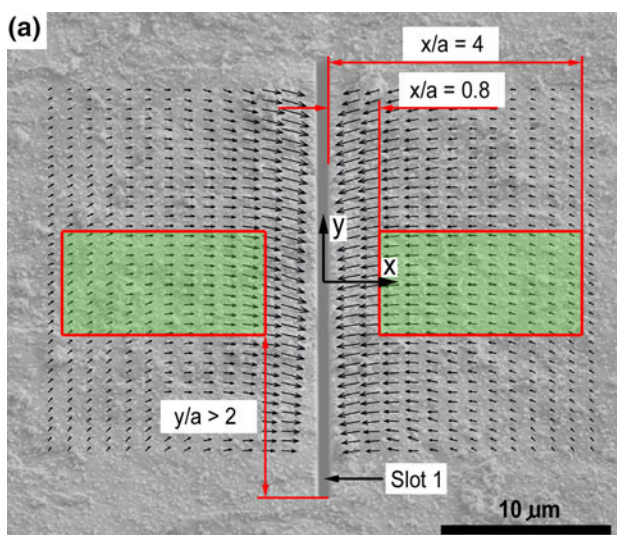


Fig. 3—(a) FEGSEM image of slot 1 (line A), with measured displacement vectors superimposed (exaggerated 25 times);  $a = 4.1 \mu\text{m}$ . (b)  $u_x$  displacements predicted for an in-plane uniaxial stress of  $-620 \text{ MPa}$  (thick red line) compared to measured average displacements (circles).

**Table III. VCPs\* Established for Region of Interest Marked in Figure 3(a) for Slot 1 (Line A)**

VCP Set	Patch Size (Pixels <sup>2</sup> )	Overlap (Pct)	Number of Passes	Global Number of Vectors**	Accuracy (nm)	$k$ (in Eq. [1]) (Pixels)
A	32 × 32	25	3	799 (105)	1.1	0.030
B	32 × 32	50	3	1798 (230)	1.0	0.028
C	64 × 64	50	3	488 (55)	0.5	0.013
D	64 × 64	75	3	1820 (230)	0.6	0.015

\*Multipass iteration technique with constant size of the subregions is used.

\*\*Number of vectors analyzed within the rectangular boxes (in Fig. 3(a)) is given in brackets.

of each microslot, images were collected before and after milling for each slot and were analyzed by DIC using the optimized VCPs.

### G. Analysis of Measured Displacements to Recover Stress

For an infinitely long, narrow slot, the displacements are given by a closed-form solution (the Inglis–Muskhelishvili solution):<sup>[24]</sup>

$$U_x = \frac{2.243}{E'} \sigma_x \int_0^a \cos \theta \left( 1 + \frac{\sin^2 \theta}{2(1-\nu)} \right) \times (1.12 + 0.18 \cdot \text{sech}(\tan \theta)) da \quad [2]$$

where  $\theta = \arctan(x/a)$ ,  $a$  is the slot depth,  $x$  is the distance from the slot,  $E' = E/(1-\nu^2)$ ,  $\nu$  is the Poisson’s ratio, and  $\sigma_x$  is the residual stress. From this, it can be seen that the displacements normal to the crack faces along the  $x$  direction are not affected by the stress  $\sigma_y$  (acting parallel to the crack).<sup>[29]</sup> In our case, the sample is represented by a linear-elastic-isotropic material:  $E = 95 \pm 5$  GPa and  $\nu = 0.37$ .<sup>[30]</sup> The results of the analytical solution are presented in Figures 4(a) and (b) for a uniaxial stress field and an equibiaxial stress field of  $-1$  GPa, respectively.

Because FIB milling does not produce ideal straight-sided infinitely long slots, finite element analysis (FEA) has been used to evaluate the extent to which this simple analytical approach is sufficient for real slots. A series of models have been compared, namely, a square-bottomed infinite slot (two-dimensional (2-D) square slot), an infinite wedge-shaped slot (2-D wedge slot), and a finite-length slot (three-dimensional (3-D) wedge slot). The wedge profile and the depth of the slot  $a$  were determined subsequent to slotting by milling an end trench (Figure 2). The results for all these simulations are displayed in Figures 4(a) and (b) for a uniaxial stress of  $-1$  GPa and an equibiaxial stress of  $-1$  GPa based on the geometry for slot 1 (line A).

All the different models show a high degree of agreement. The  $x$  displacements (along  $y = 0$ ) for the FE model of a square-bottomed slot is underestimated ( $\sim 10$  pct) for  $x/a > 3$  and overestimated by approximately 10 pct for  $x/a < 2$  by the analytical model, in agreement with the findings of Kang *et al.*<sup>[31]</sup> For a slot with triangular sides, the analytical model provides an even better description (as one might expect, given that this is more crack-like) lying within  $\sim 1.5$  pct (overestimated) to the analytical predictions for  $x/a = 1$  to 5. Closer to the slot ( $x/a < 1$ ), the analytical model overestimates the displacement (discrepancy of  $\sim 5$  pct).

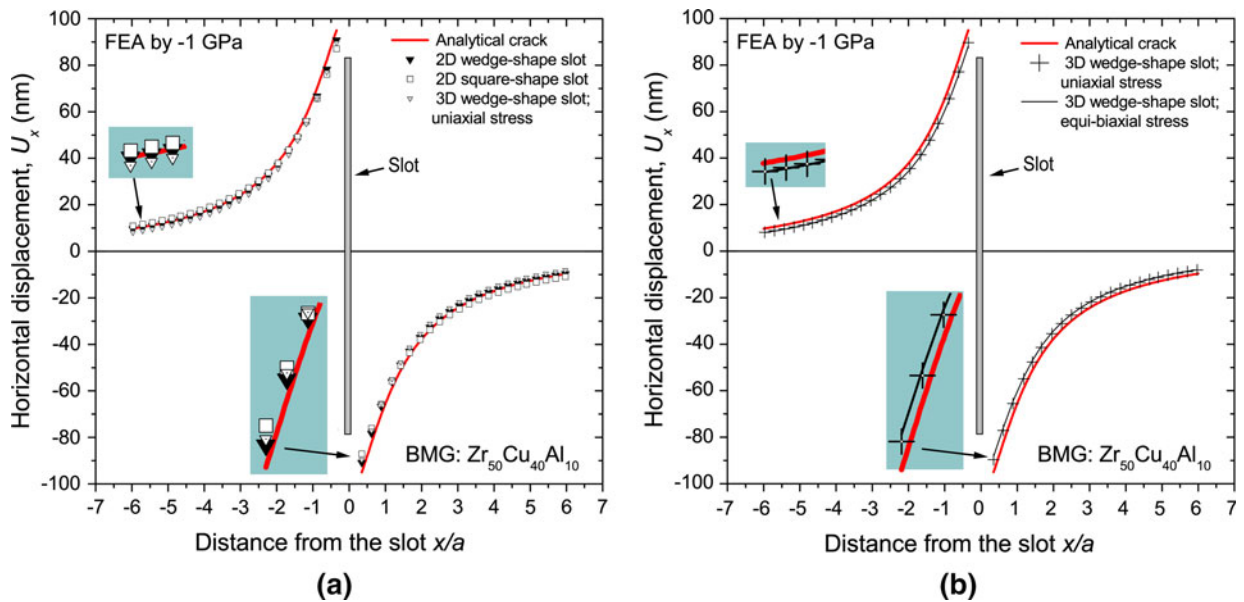


Fig. 4—Results of FEA and analytical solution (Eq. [2]) for a square-bottomed infinite slit, for the  $U_x$  displacement and  $a = 4.1 \mu\text{m}$  for (a) reference compressive uniaxial and (b) equibiaxial stress field of  $-1$  GPa for slot 1 (line A) in Fig. 1(a).

Of course, the most realistic case is the more complex 3-D analysis for a finite-length wedge-shaped slot (slot 1, line A). In this case, the analytic model overestimates the displacements by approximately 7.5 pct regardless of the distance from the slot. This means that use of the analytical form rather than the actual slot would lead to an underestimation of the stress by approximately 7.5 pct, because the displacement for a given stress is overestimated. In view of other errors associated with the measurement technique, this discrepancy is probably in itself not sufficient to require FEA modeling of each slot, although end milling is required to measure the slot depth. However, one should bear in mind that this underestimation is compounded by the fact the line  $y = 0$  is the line of maximum displacement and so if the displacement is averaged over a region over  $\pm y$ , then this underestimation of the stress will be compounded. Consequently, for shorter slots, the 3-D FE model should be used.

Figures 5(a) and (b) present the results of the 3-D FEA simulations of a slot introduced into material under the compressive uniaxial and equibiaxial stress of  $-1$  GPa. As suggested by the displacement plots in Figure 4, it confirms that the level of  $\sigma_y$  has a minimal effect on the slot-opening stress  $\sigma_x$  local to the crack. Consequently, the crack-opening displacements give a good measure of the stress  $\sigma_x$  irrespective of the strength of  $\sigma_y$ . In order to measure the other component, a second slot would be needed perpendicular to the first. In our case, the geometry of the peen/fatigue stress field is such that this was not necessary.

As mentioned previously, in order to reduce the experimental scatter in measuring  $u_x$ , the displacements within the rectangular boxes shown on either side of the

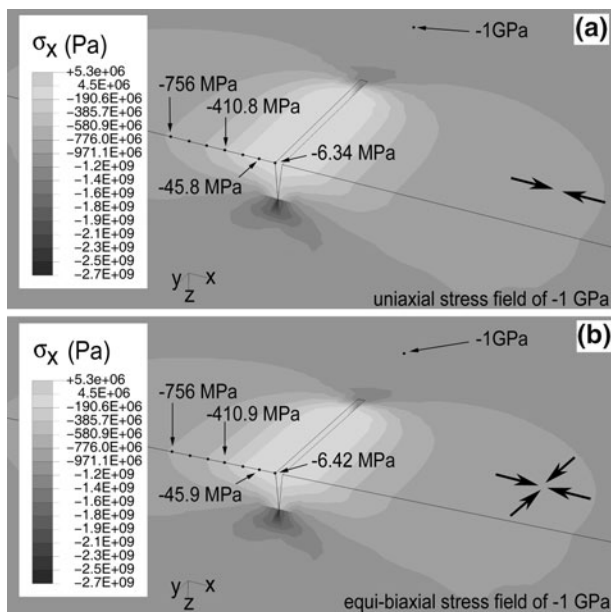


Fig. 5—Results of 3-D FEA simulations of slot 1 introduced into material that experiences (a) compressive uniaxial and (b) equibiaxial stress field of  $-1$  GPa. Both figures shows cross section in the middle of the slot and surface contour plots of stress component  $\sigma_x$ .

slit ( $-3.5 \mu\text{m} < y < 3.5 \mu\text{m}$ ) in Figure 3(a) are averaged to provide a single value of  $u_x$ . It can be seen from Figure 5 that the stress field and, hence, the displacement field is uniform with position along the crack direction over the evaluation patch ( $-3.5 \mu\text{m} < y < 3.5 \mu\text{m}$ ). In principle, it would be possible to compare full-field displacement maps with the FE predictions in order to extract the full in-plane stress field. However, given the complexity of such an analysis, the insensitivity of the  $u_x$  displacements to  $\sigma_y$  and our primary interest in the stress normal to the slit  $\sigma_x$ , the current approach is considered sufficient.

#### H. Inferring the Residual Stress

In order to determine the stress from the measured displacements, the measured average displacements  $u_x$  at each measurement location on either side of the slot  $x/a$  are plotted against the displacements expected for a  $-1$ -GPa uniaxial stress  $U_x$  calculated earlier (in our case, using the 2-D wedge-slot FEA shown in Figure 4) and a line of best fit plotted (Figure 6). Assuming totally elastic accommodation, the gradient of the best-fit line  $m$  is equal to the best-fit stress in GPa. We only analyze displacements within a certain region (defined by the green box in Figure 3(a)), because the displacements are too small further from the slot ( $x/a > 4$ ) and because redeposition of excavated material can give rise to errors closer to the slot ( $x/a < 0.8$ ).

With respect to the effect of the FIB milling process, problems associated with ion implantation in materials are well documented, *e.g.*, Reference 32. The spread and penetration range depends on the target, dopants, acceleration voltage, incident angle, *etc.* Nevertheless,

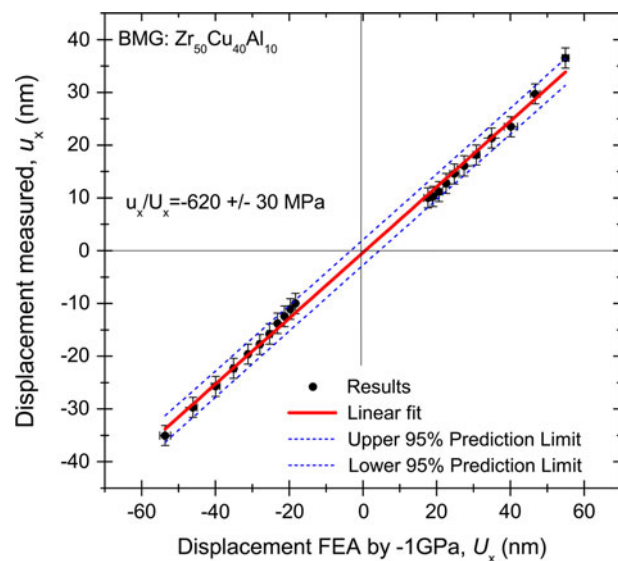


Fig. 6—Residual stress analysis for a slot of geometry corresponding to slot 1, (line A) showing measured averaged displacements,  $u_x$ , for both sides plotted against the corresponding displacements,  $U_x$ , predicted for a  $-1$ -GPa stress obtained for 2-D FE model with a triangular slot. Error bars show the root-mean-square values for DIC results at  $x$ , whereas horizontal error bars show the bounds for the FEA results. The best-fit gradient is  $0.620 \pm 0.030$ .



the Ga<sup>+</sup> ion implantation/damaged zone typically extends to a depth of the order ~15 nm at low-incidence angles (<5 deg)<sup>[33]</sup> or up to ~50 nm for normal incidence.<sup>[34,35]</sup> There are a few publications that consider the effect of ion implantation on the residual stress using cantilever techniques, *e.g.*, References 36 through 38. However, systematic studies are lacking. Residual stresses induced locally by FIB exposure have been used to fold (folding angle 0 to 180 deg) submicron-sized cantilevers/membranes (170-nm thick).<sup>[37]</sup> However, in that case, the ion irradiation volume was of the same order of magnitude as the target, creating a significant residual stress level. By contrast, a series of experiments performed on thicker cantilevers (3 μm) revealed that the effect of ion implantation on the residual stress fields is negligible (presumably due to the very shallow depth), lying within the uncertainty level for stress profiling using the microcantilever method.<sup>[38]</sup> In our case, the material volume in the vicinity of the slots is a few orders of magnitude smaller than material in which stresses are relaxed and the displacements measured and, therefore, it is likely that the effect of ion doping on the residual stress fields is negligible. The effect of redeposition has been included by taking the actual slot geometry, but if the redeposited material were significantly stressed, this might affect the measured stresses. However, we have not found significant stresses for slots in regions in which lower stress is to be expected, suggesting that this effect is not significant in our case.

As shown in Figure 6, the compressive residual stress in the *x* direction as determined by the right- and left-hand displacements for slot 1 (line A) is  $-620 \pm 30$  MPa. It can be seen from Figure 3(b) that the displacements for slot 1 correspond quite well to those predicted for a  $-620$ -MPa in-plane stress (2-D FE model with triangular slot).

### III. RESULTS

By repeating the analysis for each slot milled along the lines A and B, the profiles of the local residual stresses with depth (*z*) from the S<sup>2</sup>PD-treated surface were inferred and are presented in Figure 7.

The measured stress field along line A (expected to be unaffected by the fatigue test, because it lies outside the outermost rollers) peaks at approximately  $-670$  MPa at a depth of approximately  $160$  μm, with the compressive stresses decreasing significantly at depths greater than  $300$  μm. High compressive stresses (stress component  $\sigma_x$ ) are observed predominantly within the microstructurally affected layer (Figure 1(c)).

The residual stress distribution in the region subjected to the highest tensile fatigue amplitude (line B) is also shown. The compressive stresses within the microstructurally affected peened layer are significantly reduced by approximately 75 pct to value approximately  $-170$  MPa. Immediately beneath the microstructurally affected peened layer (at a depth of approximately  $250$  μm), the stresses are reduced by approximately 15 pct during the fatigue test. At depths beyond  $300$  μm, the compressive stresses are small for both depth profiles, with the

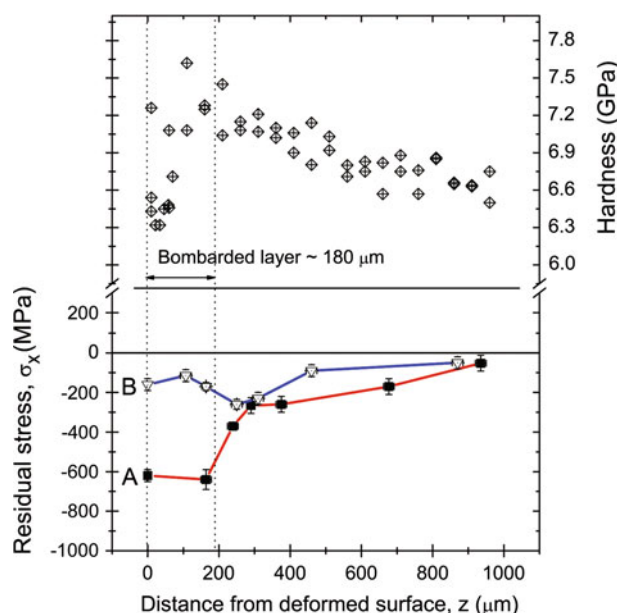


Fig. 7—Inferred local residual in-plane stress ( $\sigma_x$ ) profiles along lines A and B in Fig. 1(a) as a function of depth from the deformed surface (bottom) and the hardness values obtained from Ref. 27 (top).

fatigue-affected region slightly lower than the as-peened material.

### IV. DISCUSSION

The measured stress field in the region of the specimen unaffected by the fatigue test is characteristic of shot-peening profiles (for example, References 9 and 12). The peak compressive residual stress introduced by the S<sup>2</sup>PD surface treatment process is located within the microstructurally affected layer at approximately a  $180$ -μm depth (Figure 7), although it appears to vary little across this region. The form of our stress profile is in good agreement with Mear *et al.*,<sup>[12]</sup> who analyzed as-peened Zr<sub>55</sub>Ti<sub>5</sub>Al<sub>10</sub>Cu<sub>20</sub>Ni<sub>10</sub> BMG (at. pct) using an analysis of diffuse synchrotron X-ray scattering, the microstructurally evident depth being, in their case, approximately  $160$  μm. Further, they found that the stresses extended to a depth of approximately  $270$  μm, in close agreement with our findings ( $\sim 300$  μm). They reported that in the microstructurally evident surface region, the effective strains suggest a plastic-strain-induced volume change of the order of 1 pct, meaning that in this region, the atomic spacing cannot be interpreted simply in terms of stress without serious error. This stress-free change in the atom spacing severely complicates the interpretation of the X-ray scattering method near the surface. Instead, in their case, the near-surface stresses must be inferred from the profile below the microstructurally evident depth. It is noteworthy that despite the differences between our approaches, we have arrived at similar conclusions. In our case, the peen stresses are significantly below the bulk yield stress of 1.86 GPa;<sup>[27]</sup> this may in part be due to the near-surface softening caused by the peening action (Figure 7).<sup>[27]</sup>

It is clear that the residual stress profile in the as-peened state correlates with the hardness profile also shown in Figure 7, measured previously,<sup>[27]</sup> namely, that the hardness and the compressive residual stress increase to a depth of approximately 150  $\mu\text{m}$ , and then decrease toward the value representative of the substrate at greater depths. Raghavan *et al.*<sup>[10]</sup> and Steif *et al.*<sup>[39]</sup> report strain softening in the very-near-surface region ( $\sim 30 \mu\text{m}$ ), also seen here. In the absence of dislocations, work hardening is difficult. Consequently, it is believed that the hardness variations with depth are related primarily to the residual stresses. Indeed, a correlation between the hardness and residual stress has been reported in other systems.<sup>[9–11]</sup> For example, Chen *et al.*<sup>[11]</sup> found that the nominal hardness of a BMG specimen is strongly dependent on the residual stress state, *i.e.*, the hardness decreases with a tensile residual stress but increases with a compressive residual stress. In crystalline materials, this relation has been used to characterize the residual stress by indentation testing.<sup>[40,41]</sup>

During the fatigue testing, the peened surface experiences cyclic tensile loading, attaining a peak load of 500 MPa. The influence of the fatigue process on the residual stress distribution is clearly evident. Compressive residual stresses (stress component  $\sigma_x$ ) are considerably reduced by approximately 75 pct within the microstructurally affected layer. The peening process clearly introduces beneficial compressive residual stresses in metallic glass to a depth of approximately 300  $\mu\text{m}$ . At the same time, peening introduces severe plastic deformation with multiple fine shear bands and often microcrack regions (Figure 8), which are nuclei for residual stress-relaxation processes and subsequent fracture events during fatigue. It should be pointed out that this study considers only the in-line residual stress component  $\sigma_x$  parallel to the loading axis.

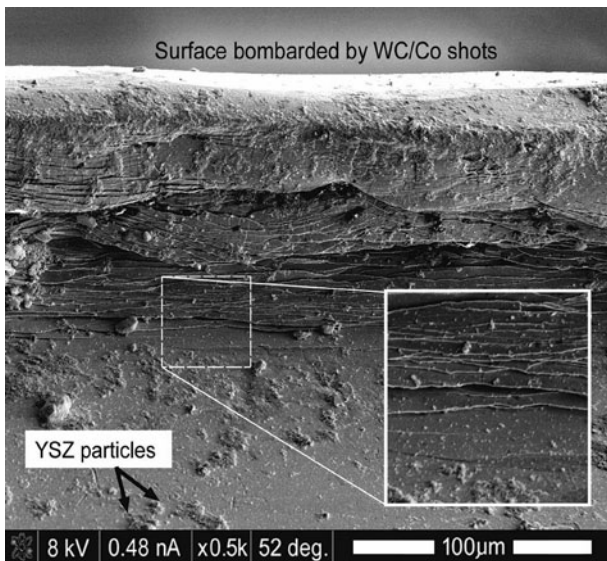


Fig. 8—FEGSEM image showing microstructurally affected layer with multiple fine shear bands.

It was observed that in the peened layer, residual shear stresses exist. Thus, to sufficiently understand the influence peening and fatigue processes on residual stress distribution in BMGs, it is essential to analyze more components of residual stress with reference to the distribution and orientation of fine shear bands.

## V. CONCLUSIONS

In summary, this article has presented a new method for mapping the residual stress of amorphous materials as a function of position at the micron scale. The potential applications of this technique include the measurements of the residual stresses of amorphous thin films, micromachined components and devices, nanostructured materials, *etc.* Although applicable to crystalline materials, for amorphous materials, the microslotting method has few competitors, being especially useful for characterizing the near-surface residual stress in which hole drilling is difficult to perform<sup>[42]</sup> or in which a high depth or lateral spatial resolution is required.

It is recommended to verify the actual dimensions of the slot for the following two reasons: (1) the actual depth of the slot needs to be accurately known and (2) the shape of the slot becomes important when its length is short.

Through FE modeling, we found that the simpler infinite-wedge-slot model was within 3.5 pct of the more representative 3-D wedge-shaped-slot model, and that the analytical model was good to within 7.5 pct. Consequently, simple models can be used in most cases, except for very short or shallow slots. The modeling has shown that the stresses  $\sigma_x$  and  $\sigma_y$  are negligibly coupled for elastic deformations so that the stress  $\sigma_x$  can be measured without having to consider  $\sigma_y$ .

It is insightful to compare this current study to the measurement of stresses in a similar BMG by X-ray scattering.<sup>[12]</sup> As a mechanical method, in contrast to X-ray scattering methods, it is not particularly sensitive to local atomic volume changes caused by the plastic work. Meer *et al.*<sup>[12]</sup> demonstrated that in the plastic (microstructurally affected) zone (160  $\mu\text{m}$ ), large changes in atomic spacing ( $\sim 1$  pct) were observed that were not macrostress related (this equates to an  $\sim 800$ -MPa stress error), ruling out the possibility of using this method to measure the stress in the plastic zone. While our method is sensitive to changes in modulus, these changes are estimated to be of the order of a few percent. Overall, our mechanical measurements are consistent with the results of Meer *et al.*,<sup>[12]</sup> both those measured in the elastic region and those inferred in the microstructurally affected zone. In the present S<sup>2</sup>PD BMG case, the severely plastically deformed layer is confined to within 180  $\mu\text{m}$  of the surface but has considerable influence on the overall mechanical properties of the component. Our method provides a simple and cost-effective way of mapping the residual stress profile. Compared with the curvature measurement of the layer removal method, the slotting method is much easier to apply to near-surface treatments, and the measurement accuracy is



shown to be ~30 MPa, even for such a stiff BMG material.

The S<sup>2</sup>PD surface treatment process introduced beneficial compressive residual stresses within the microstructurally affected layer. Stresses reached a peak of approximately -670 MPa toward the boundary of the microstructurally affected zone ( $z = 160 \mu\text{m}$ ) and the elastically restraining parent, with the compressive stresses decreasing significantly at depths greater than 300  $\mu\text{m}$ .

The fatigue process considerably reduced compressive residual stresses within the microstructurally affected layer by a factor of approximately 3.5. In this article, we have focused on one component of the stress field ( $\sigma_x$ ); while in principle it would be possible to extend this method to a full-field in-plane analysis, other methods may be more appropriate for such a task. In a forthcoming article, we describe a new microhole-drilling method<sup>[43]</sup> better suited to this purpose.

### ACKNOWLEDGMENTS

The stress measurements were made within the Stress and Damage Characterization Unit at the University of Manchester supported by the Light Alloys Towards Environmentally Sustainable Transport (LATEST) Engineering and Physical Sciences Research Council (EPSRC) Portfolio Project. Two of the authors (JT and PKL) are supported by the National Science Foundation International Materials Institutes (IMI) and Combined Research and Curriculum Development (CRCD) Programs, Tennessee. The nanoindentation results were obtained from Reference 27 and were developed by Professor L.L. Shaw of the University of Connecticut, Connecticut.

### REFERENCES

1. A.L. Greer: *Nature*, 1999, vol. 402, pp. 132–33.
2. D.C. Hofmann, J.Y. Suh, A. Wiest, G. Duan, M.L. Lind, M.D. Demetriou, and W.L. Johnson: *Nature*, 2008, vol. 451, pp. 1085–89.
3. W.L. Johnson: *MRS Bull.*, 1999, vol. 24, pp. 42–56.
4. A. Inoue, I. Yoshii, H. Kimura, K. Okumura, and J. Kurosaki: *Mater. Trans.*, 2003, vol. 44, pp. 2391–95.
5. J. Das, M.B. Tang, K.B. Kim, R. Theissmann, F. Baier, W.H. Wang, and J. Eckert: *Phys. Rev. Lett.*, 2005, vol. 94, pp. 205501–205504.
6. G.Y. Wang, P.K. Liaw, W.H. Peter, B. Yang, Y. Yokoyama, M.L. Benson, B.A. Green, M.J. Kirkham, S.A. White, T.A. Saleh, R.L. McDaniels, R.V. Steward, R.A. Buchanan, C.T. Liu, and C.R. Brooks: *Intermetallics*, 2004, vol. 12, pp. 885–92.
7. M.F. Ashby and A.L. Greer: *Scripta Mater.*, 2006, vol. 54, pp. 321–26.
8. C.C. Aydiner and E. Ustundag: *Mech. Mater.*, 2005, vol. 37, pp. 201–12.
9. Y. Zhang, W.H. Wang, and A.L. Greer: *Nat. Mater.*, 2006, vol. 5, pp. 857–60.
10. R. Raghavan, R. Ayer, H.W. Jin, C.N. Marzinsky, and U. Ramamurty: *Scripta Mater.*, 2008, vol. 59, pp. 167–70.
11. L.Y. Chen, Q. Ge, S. Qu, and J.Z. Jiang: *Scripta Mater.*, 2008, vol. 59, pp. 1210–13.
12. F.O. Mear, G. Vaughan, A.R. Yavari, and A.L. Greer: *Philos. Mag. Lett.*, 2008, vol. 88, pp. 757–66.
13. P.J. Withers: *Rep. Prog. Phys.*, 2007, vol. 70, pp. 2211–64.
14. R. Gardon: *Elasticity and Strength in Glasses*, Academic, New York, NY, 1980, pp. 145–216.
15. C.C. Aydiner, E. Ustundag, and J.C. Hanan: *Metall. Mater. Trans. A*, 2001, vol. 32, pp. 2709–15.
16. C.C. Aydiner, E. Ustundag, M.B. Prime, and A. Peker: *J. Non-Cryst. Solids*, 2003, vol. 316, pp. 82–95.
17. R.D. Conner, W.L. Johnson, N.E. Paton, and W.D. Nix: *J. Appl. Phys.*, 2003, vol. 94, pp. 904–11.
18. A. Turnbull, J.J. Pitts, and J.D. Lord: *Mater. Sci. Technol.*, 2008, vol. 24, pp. 327–34.
19. H.F. Poulsen, J.A. Wert, J. Neuefeind, V. Honkimaki, and M. Daymond: *Nat. Mater.*, 2005, vol. 4, pp. 33–36.
20. J. Das, M. Bostrom, N. Mattern, A. Kvick, A.R. Yavari, A.L. Greer, and J. Eckert: *Phys. Rev. B*, 2007, vol. 76, pp. 092203-1–092203-4.
21. P.J. Withers and H. Bhadeshia: *Mater. Sci. Technol.*, 2001, vol. 17, pp. 355–65.
22. P.J. Withers, M. Turski, L. Edwards, P.J. Bouchard, and D.J. Buttle: *Int. J. Pressure Vessels Pip.*, 2008, vol. 85, pp. 118–27.
23. O.E. Kongstein, U. Bertocci, and G.R. Stafford: *J. Electrochem. Soc.*, 2005, vol. 152, pp. C116–C123.
24. H. Tada, P. Paris, and G. Irwin: *The Stress Analysis of Cracks Handbook*, PEP, Bury St. Edmunds, UK, 2000, pp. 82–96.
25. K.J. Kang, N. Yao, M.Y. He, and A.G. Evans: *Thin Solid Films*, 2003, vol. 443, pp. 71–77.
26. N. Sabate, D. Vogel, A. Gollhardt, J. Keller, C. Cane, I. Gracia, J.R. Morante, and B. Michel: *J. Micromech. Microeng.*, 2006, vol. 16, pp. 254–59.
27. J.W. Tian, L.L. Shaw, Y.D. Wang, Y. Yokoyama, and P.K. Liaw: *Intermetallics*, 2009, vol. 17 (11), pp. 951–57.
28. J. Quinta De Fonseca, P.M. Mummery, and P.J. Withers: *J. Microsc.*, 2004, vol. 218, pp. 9–21.
29. A.N. Guz: *Int. Appl. Mech.*, 2000, vol. 36, pp. 1537–64.
30. J.M. Pelletier, Y. Yokoyama, and A. Inoue: *Mater. Trans.*, 2007, vol. 47, pp. 1359–62.
31. K.J. Kang, S. Darzens, and G.-S. Choi: *J. Eng. Mater. Technol.*, 2004, vol. 126, pp. 457–64.
32. M. Nastasi and J.W. Mayer: *Ion Implantation and Synthesis of Materials*, Springer-Verlag, Berlin-Heidelberg, 2006, pp. 49–61.
33. J.F. Ziegler, J.P. Biersack, and U. Littmark: *The Stopping Range of Ions in Matter*, Pergamon Press, New York, NY, 1985, pp. 67–78.
34. S. Lipp, L. Frey, C. Lehrer, B. Frank, E. Demm, and H. Ryssel: *J. Vac. Sci. Technol.*, 1996, vol. 14, pp. 3996–99.
35. B.W. Kempshall and L.A. Giannuzzi: *J. Vac. Sci. Technol.*, 2002, vol. 20, pp. 286–90.
36. T.J. Kang, J.G. Kim, J.S. Lee, J.H. Lee, J.H. Hahn, H.Y. Lee, and Y.H. Kim: *J. Micromech. Microeng.*, 2005, vol. 15, pp. 2469–78.
37. W.J. Arora, H.I. Smith, and G. Barbastathis: *Microelectron. Eng.*, 2007, vol. 84, pp. 1454–58.
38. S. Massl, J. Keckes, and R. Pippan: *Acta Mater.*, 2007, vol. 55, pp. 4835–44.
39. P.S. Steif, F. Spaepen, and J.W. Hutchinson: *Acta Metall.*, 1982, vol. 30, pp. 447–55.
40. S. Carlsson and P.L. Larsson: *Acta Mater.*, 2001, vol. 49, pp. 2179–91.
41. X. Chen, J. Yan, and A.M. Karlsson: *Mater. Sci. Eng. A.*, 2006, vol. 416, pp. 139–49.
42. W. Cheng and I. Finnie: *Residual Stress Measurement and the Slitting Method*, Springer, New York, NY, 2007, pp. 123–35.
43. B. Winiarski and P.J. Withers: Unpublished research.